JACS
JOURNAL OF THE AMERICAN CHEMICAL SOCIETY

Article

Room Temperature Dual Fluorescence of a Locked GFP Chromophore Analogue

Soumit Chatterjee, Ketan Ahire, and Peter Karuso

J. Am. Chem. Soc., **Just Accepted Manuscript** • DOI: 10.1021/jacs.9b05096 • Publication Date (Web): 17 Dec 2019

Just Accepted

is published by the American Chemical Society. 1155 Sixteenth Street N.W., Washington, DC 20036

Room Temperature Dual Fluorescence of a Locked GFP Chromophore Analogue.

Soumit Chatterjee,§ Ketan Ahire and Peter Karuso*

Department of Molecular Sciences, Macquarie University, Sydney, NSW 2109, Australia

KEYWORDS: GFP, dual emission, ratiometric, fluorescence, ESIPT, confocal microscopy, upconversion, DFT.

ABSTRACT: A structurally locked GFP chromophore with a phenyl group at C(2) of the imidazolone has been synthesized. Rotation around the exocyclic double bond is hindered, resulting in room temperature fluorescence. The quantum yield in water is 500 times greater than that of unlocked analogues. Unlike the methyl-substituted analogue, the phenyl analogue exhibits a dual emission (cyan and red) that can be used for ultrasensitive ratiometric measurements and fluorescence microscopy. To explain this dual emission, DFT calculations were carried out along with fluorescence upconversion experiments. The *Z*-isomer was found to be emissive, while the origin of the dual emission was dependent on the phenyl group in the *Z*-isomer, which stabilizes the Franck-Condon state, resulting a cyan fluorescence while the zwitterionic tautomer fluoresces red. These results bring important new insights into the photophysics of the GFP chromophore and provide a new scaffold capable of dual emission with utility in biotechnology.

INTRODUCTION

Green fluorescence protein (GFP) is widely used in molecular biology and biotechnology as a genetically encoded fluorescent tag.[1] Its strong green fluorescence ($\phi_f = 0.8$) is ascribed to its chromophore 4-(4-hydroxybenzylidene)-1,2-dimethyl-1*H*-imidazol-5(4*H*)-one (*p*-HBDI, Chart 1), which is conformationally locked by covalent and hydrogen bonds inside the β-barrel structure of the protein.[2] The photophysics of GFP involves excited state proton transfer (ESPT) to the E222 residue, through a proton relay. The resulting anionic excited state of *p*-HBDI is believed to be responsible for the observed green fluorescence.[3] In 2002, Remington observed GFP mutants (*e.g.* H148G, T203C; deGFP) that display dual blue/green emission that is pH sensitive.[4] This was attributed to perturbation of the ESPT such that both the normal Franck-Condon (FC) and ESPT emissions are observed. The design and synthesis of small molecules that mimic the dual emission of deGFP could find a range of applications in chemistry and biology that require ratiometric sensing and in super resolution microscopy if the dual emission can be switched.[5]

Chart 1. Structure of the GFP chromophore and conformationally restricted analogues

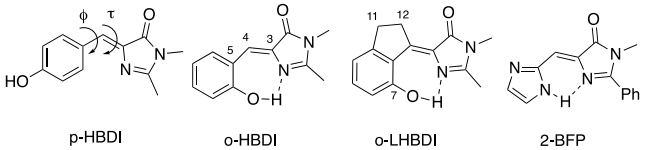

Dual emission is a rare property in fluorescent molecules but can arise in aromatic dyes where there is a strong electron donor-acceptor pair that participate in an excited state intramolecular charge transfer (ICT) or a twisted intramolecular charge transfer (TICT).[6] The problem though is that it is difficult to get two-band emission of similar intensities because the ICT is prone to strong quenching.[7] In fluorophores that contain both a H-bond donor and acceptor in close proximity, it is also possible to have an excited state intramolecular proton transfer (ESIPT) in which both tautomers establish an equilibrium and display two emissions with similar intensities.[8] In these cases, it is possible to produce truly ratiometric dyes that are sensitive to their environment.[9]

It is well known that the isolated chromophore of GFP (*p*-HBDI) is essentially non-fluorescent at room temperature ($\phi_f < 0.001$)[10] due to facile photoisomerization (Scheme S1; Supporting Information), resulting in an internal conversion to the ground state within 1 ps.[11] The design of small molecule ratiometric fluorophores based on HBDI thus faces the dual challenge of minimizing photoisomerization and converting the ESPT of GFP into an ESIPT. Our design elements to achieve this included moving the hydroxyl group into the ortho-position (*o*-HBDI) for an ESIPT and introduction of a five membered ring to hinder ϕ/τ rotation (Chart 1)[10b,10c,12]. These approaches have been combined by Chou and co-workers to produce (*o*-LHBDI; Chart 1) with a dramatic enhancement of fluorescence at room temperature ($\phi_f = 0.18$ in toluene).[8a] However, no dual emission was observed and the compound appears to not be fluorescent in water – a prerequisite for biological application. In contrast, an analogue of the chromophore from the blue fluorescent protein (2-BFP) displayed dual fluorescence in non-polar solvents but again appeared to be non-fluorescent in water and displayed only a single week emission in methanol. Computational results suggested that two competitive S_1 relaxation pathways from the Franck–Condon point in non-polar solvents led to normal (470 nm) and ESIPT (595 nm) emissions.[13]

Scheme 1. Synthesis of *o*-LHBPI[a]

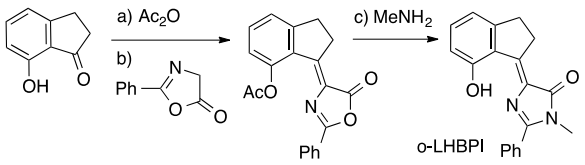

[a] Reagents and conditions: (a) Ac_2O, NaOAc (2.0 equiv), μwave 300W, 140 °C, 3 min, 97%; (b) phenyloxazolinone (1.6 equiv.), $TiCl_4$ (1.0 equiv.)/THF, –10 °C, 20 min; then pyridine, 5 h, 40%; (c) 40% aqueous $MeNH_2$, K_2CO_3 (1 equiv.) reflux, 3 h, 40%.

Herein we report the synthesis and photophysics of *o*-LHBPI (*o*-**l**ocked **h**ydroxy**b**enzylidene-*p*-**p**henyl-**i**midazolinone; Scheme 1), which has a dual emission at room temperature that is sensitive to the local environment. This is remarkably different from *o*-LHBDI that has a single emission at 600 nm attributed to the zwitterion tautomer formed via ESIPT.[8a] The unique characteristics of *o*-LHBPI could be used for chemical sensing, fluorescence cell imaging, optoelectronic devices, two color light emitting diodes or for super high resolution microscopy (*e.g.* STORM).

RESULTS AND DISCUSSION

The synthesis of *o*-LHBPI (Scheme 1) was simple but non-trivial as the typical Erlenmeyer–Plöchl azlactone synthesis used for HBDI analogues, which works well for aldehydes, fails for ketones. After some experimentation, we independently came up with a solution similar to that of Chou,[8a] utilizing $TiCl_4$ as a Lewis acid but with the oxazolinone (Scheme 1, step b) instead of the imidazolone used by Chou. This has two advantages; firstly, the oxazolinone is easily formed in one step from hippuric acid and secondly deprotection and conversion to the imidazolinone can be achieved in one step with aqueous methylamine.[14] This is a significant improvement on the two-step approach previously published that involved reaction with dry methylamine in DCM to produce the ring-opened *o*-LHBPI, which precipitated out and could be filtered and cyclized by heating under vacuum to afford the final product.[15] The compound was purified by HPLC and shown to be homogeneous by LC-MS (Fig. S1) and NMR spectroscopy (Fig. S2-5).

It is theoretically possible to have τ-bond E- and Z-isomers of *o*-LHBDI where the phenol H-bonds to the carbonyl or nitrogen of the imidazolone respectively. A quantitative solution structure of *o*-LHBDI was carried out by first constructing an NOE buildup curve (Fig. S6) from the NOSEY data (Fig. S7). Comparison of the measured interatomic distances (Table S1) in comparison with the DFT optimized structures (Table S2) showed conclusively that in $CDCl_3$, only Z-*o*-LHBDI is observed. Specifically, the size of the NOE between the phenol and ortho-proton on the phenyl ring are not consistent with E-*o*-LHBDI.

The absorption spectra of *o*-LHBPI exhibit two overlapping peaks at ~370 nm and ~410 nm in all the solvents studied (Fig. 1, Fig. S8). The small solvent effect suggests these arise from delocalized π-π* transitions. These are in good agreement with the absorption lines (365 and 410 nm) predicted for *Z*-*o*-LHBPI by TD-DFT calculations in water (Fig. 2A red line). Rotation of τ by 180° (Chart 1) yields *E*-*o*-LHBPI, which is predicted to have a qualitatively similar UV spectrum (Fig. 2 gold line) except the 365 nm band is shifted to 375 nm. The anionic (Fig. 2A brown line) shows a shift of the 410 nm band to 360 nm and a new quinoid-type band at~480 nm (*c.f.* catechol; 276 nm B-band goes to 247 and 389 nm K- and R-bands respectively)[16], which is not observed in the experimental absorption spectrum. The phenol C(6)–O bond length in the ground state is calculated to be 1.255 Å for the anion and 1.330 Å in the neutral form. Similarly, the C(4)–C(5) bond length is shorter in the anion ion (1.431) compared to the neutral form (1.447 Å) suggesting more of an ortho-quinonemethide contribution to the ground state in the anion. The DFT calculations of the neutral form were in good agreement with the 400 nm absorption but the low oscillator strength of the 370 nm band suggests that DFT calculations, at this level of theory, are not ideal for predicting the intensity of the second absorption or that there is some percentage of the anionic form in the ground state and that it is in rapid equilibrium with the neutral tautomers. Coupled cluster (SOS-CC2//TZVPP) calculations gave the same two absorptions but closer in oscillator strength (Fig. 2B).

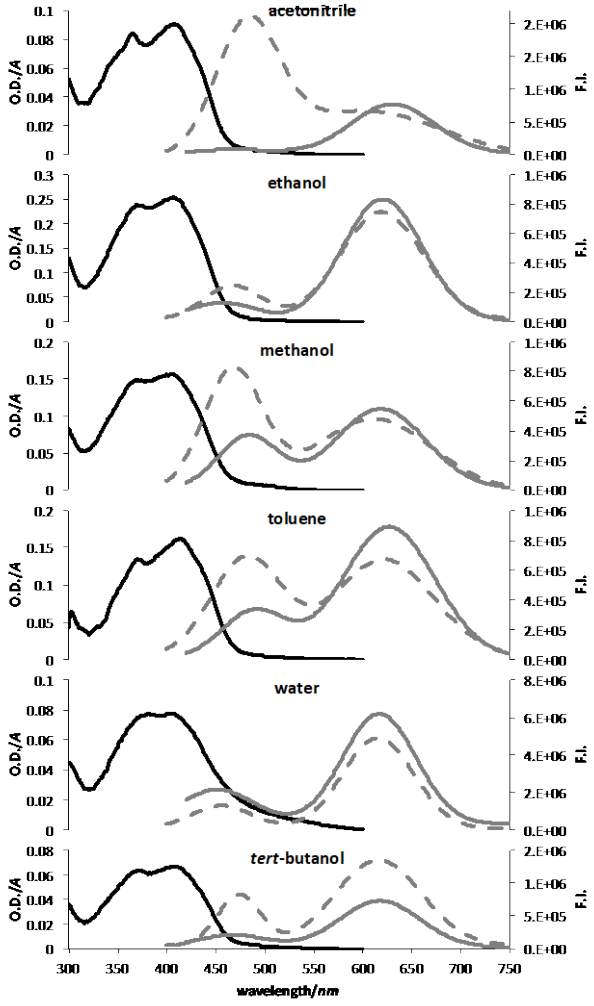

Figure 1. Steady state absorption (black) and emission spectra (grey) for *o*-LHBPI. Emission spectra with excitation at 370 nm (dashed) and 410 (solid) are shown for six solvents.

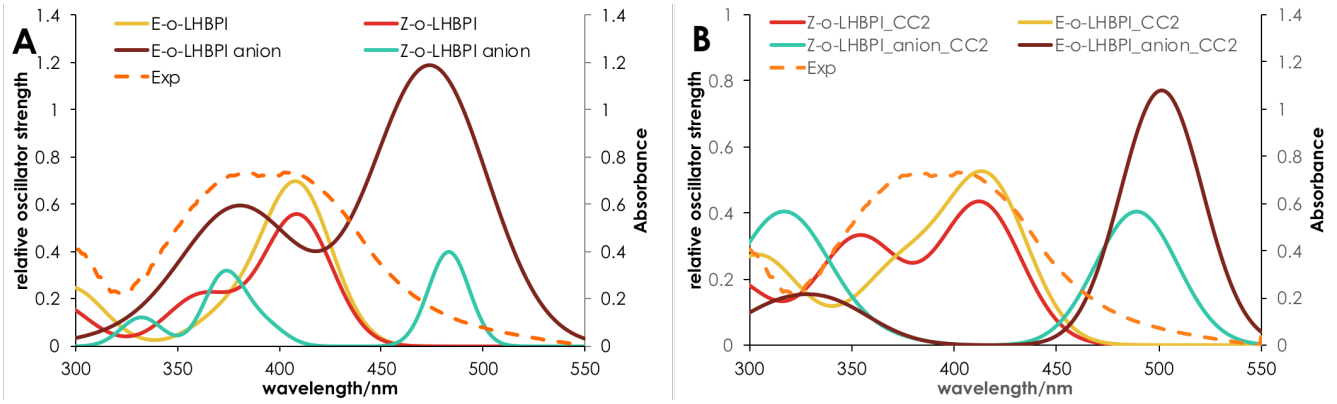

Figure 2. Calculated absorption lines for *o*-LHBPI isomers and tautomers in water. A) TD-DFT//pbe0/TZVPP-COSMO) for the *E*-, *Z*- and anionic forms. Calculated lines are Gaussian broadened by 16 nm and shifted +10 nm to facilitate comparison with the experimental spectrum (Exp) in water. B) Same as A) except ab initio coupled cluster calculations (SOS-CC2/TZVPP). See Table S3 for TD-DFT and SOS-CC2 wavelengths and oscillator strengths.

While the absorption spectra of *o*-LHBPI and *o*-LHBDI are qualitatively similar, the emission spectra are not. For *o*-LHBPI, a dual emission at 475 (cyan) and 610 (red) nm is observed (Fig. 1, Fig. S9), similar to other analogues, recently reported by Mandal and co-workers.[12f] The origin of the 475 and 610 nm bands can be attributed to normal Franck Condon (FC) emission and an emissive state arising from an ESIPT respectively.[8a,12f] Surprisingly, the relative fluorescence quantum yield of the ESIPT band is greatest in water (Table S4). This is surprising because ESIPT is usually hindered by the formation of "blocked" structures in protic solvents,[17] but can be rationalized by the involvement of water in a proton relay, facilitating the ESIPT as is seen in deGFP proteins.[4] Such phenomena have also been previously reported for unrelated systems.[18] DFT calculations of a water complex (Fig. S10) show that this is at least possible. In the ground state, water can act as a H-bonding bridge and that in S_1 there is a water relayed ESIPT that was able to be simulated without any constraints.

The differences in emission resulting from excitation at 370 nm and 410 nm (Fig. 1) suggests heterogeneity in the ground state. This is especially evident in acetonitrile and methanol where excitation at 370 nm results in primarily cyan emission and excitation at 410 nm results in more red emission. NMR spectroscopy (Figs S4-S5) and HPLC (Fig. S1) confirmed the compound was pure and homogeneous so any heterogeneity must be in rapid equilibrium on the NMR time scale. Looking at the excitation spectrum in methanol (Fig. 3), monitored at λ_{em} = 610 nm gave a good match for the absorption spectrum (Fig. 3A, blue line) but monitored at λ_{em} = 475 nm (Fig. 3A, green line) gave a poor match for the absorption spectrum with a peak at ~360 nm, which is the position of the higher energy absorption maximum. To deconvolute this, the absorption and fluorescence excitation spectra were fitted to a sum of three Gaussian functions. One Gaussian was held fixed at 267 nm corresponding to the benzenoid band, the onset of which can be seen in the absorption as well as excitation spectra. Fitting of the absorption spectrum (Fig. 3B, red line) gave an excellent match to two absorptions at 360 and 412 nm. Fitting the excitation spectrum, monitored at the 610 nm emission (Fig. 3C, red line) results in exactly the same two absorptions but in a different ratio. Monitoring the excitation spectrum with an emission at 475 nm (Fig. 3D, green line) again results in the same two Gaussians but now dominated by the 360 nm peak. Fitting of all three curves predicted the absorption and excitation spectra are composed of two transition of 364 ± 4 nm and 415 ± 3 nm as predicted from DFT and ab initio calculations (Fig. 2). The onset of the excitation spectra for the two emissions in Fig. 3A also suggested heterogeneity in the ground state. In methanol this could be due to the formation of solvent adducts or the anion. To investigate this, excitation spectra of *o*-LHBPI in toluene (Fig. S11) were obtained and found to be similar to methanol (Fig. 3A), suggesting that the ground state heterogeneity is not due to solvent, the anion or H-bonding but could be due to cis-/trans- isomerism of the τ-bond.

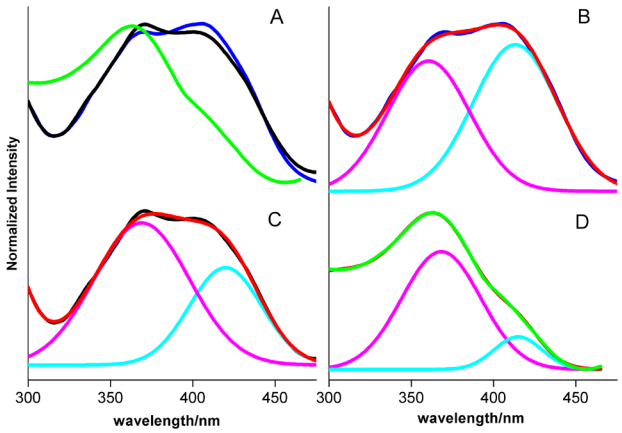

Figure 3. Fitting of Gaussians to absorption and excitation spectra. A) Normalized absorption (blue) and excitation spectra in methanol. λ_{em} = 475 nm (green) and λ_{em} = 610 nm (black). B) Absorption spectrum (blue) as a sum of three-Gaussian functions (red), one fixed at 267 nm, not shown. C) Excitation spectrum (λ_{em} = 610 nm, black) as a sum of three-Gaussian functions (red). D) Excitation spectrum (λ_{em} = 475 nm, green) as a sum of three-Gaussian functions (red).

Measurements under basic conditions (Fig. S12) confirmed that the anion has an emission at 475 nm that begins to dominate the emission spectrum after pH 9 (Fig. S12A) but even at pH 12, there is still a red emission (Fig. S12B). This was repeated in a non-protic solvent (2-methyltetrahydrofuran; MeTHF) to confirm that addition of TFA quenches cyan emission and addition of excess sodium hydroxide leads to strong cyan emission but no change to the red emission (Fig. 4). While the anion

is clearly responsible for the cyan emission, it too shows dual emission, probably via a solvent mediated ESPT. Interestingly, excitation of the anion at 370 nm or 410 nm leads to the same red emission but different levels of cyan emissions (Fig. 4).

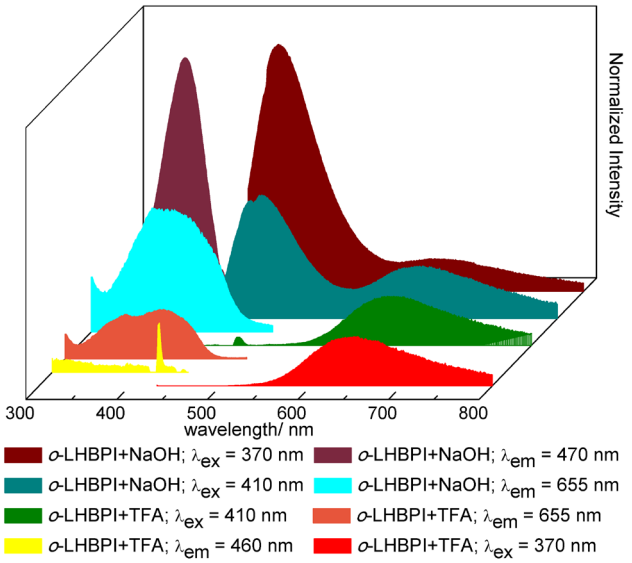

Figure 4. Response of o-LHBPI to acid and base in a non-protic solvent. Normalized excitation and emission traces of o-LHBPI in MeTHF with the addition of TFA or 25% NaOH.

The absorption spectrum of *o*-LHBPI is not affected significantly by pH, except for the appearance of a ~40 nm red shifted band at pH = 12 (Fig. S13), marking the formation of the anionic ground state of the molecule (*c.f.* Fig. 2, dark red line, Fig. S13, S14). The ESIPT emission band is suppressed above pH 10, due to deprotonation of the phenol as expected (Fig. S12). It was not possible to measure the ground state pK_a because the absorption spectrum is independent of pH except above pH 12 and at higher pH there is evidence of decomposition, but the emission spectra were pH dependent and it was possible to measure a pK_a* (Fig. S15) of around 9. Interestingly, regardless of what excitation wavelength was used or what emission was observed, the calculated pK_a* was the same, suggesting a lack of heterogeneity in the excited state.

An initial study of the temporal dynamics of the two-band emission was performed by femtosecond time resolved fluorescence measured in a time window of 500 picoseconds. Femtosecond fluorescence transients at 475 nm are identical for excitation wavelengths of 370 nm and 410 nm and are complete within 2 ps (Fig. 5, Table S5), which is consistent with a short-lived FC emission.[8a,12f] The radiative rate constants calculated from the lifetime values for 475 nm emission (Table S5) are found to be in the order of 10^8 s^{-1}, very high but consistent with previously reported radiative rate constants of other organic molecules.[11e,11i,19] However, in water and in toluene, the radiative rate constants are found be two orders of magnitude higher than HBDI and its analogues.[11e,11i,19c] We believe, as the sum-frequency wavelength generated from 820 nm and 475 nm is very close to the SFG wavelength originating from the solvent Raman peak (*i.e.* the cross-correlation function used for measuring instrumental resolution), we are unable to separate the Raman peak from the emission. Therefore, the 475 nm emission decay traces are probably unreliable, also noting that the deconvoluted results are below the resolution of the instrument. Unfortunately, the wavelength and resolution are limitations of the instrumentation available.

For an excitation at 410 nm, the transient at 610 nm in water is over within 300 ps, and is significantly slower than that at 475 nm. It is tempting to assign the fastest component (300 fs, Table S5) found in aqueous solution to the proton transfer process.[12f] However, no rise time is observed for the 610 nm emission suggesting the proton transfer is fast (< 280 fs) and thus not resolved with our instrumental set-up. The decays, except those in aqueous solution, are biexponential, with components in the picosecond and tens of picosecond regimes. The additional sub-picosecond component is found only in aqueous solutions, possibly indicating the involvement of hydrogen bond dynamics in the excited state of the molecule preferring ESPT over ESIPT.[18]

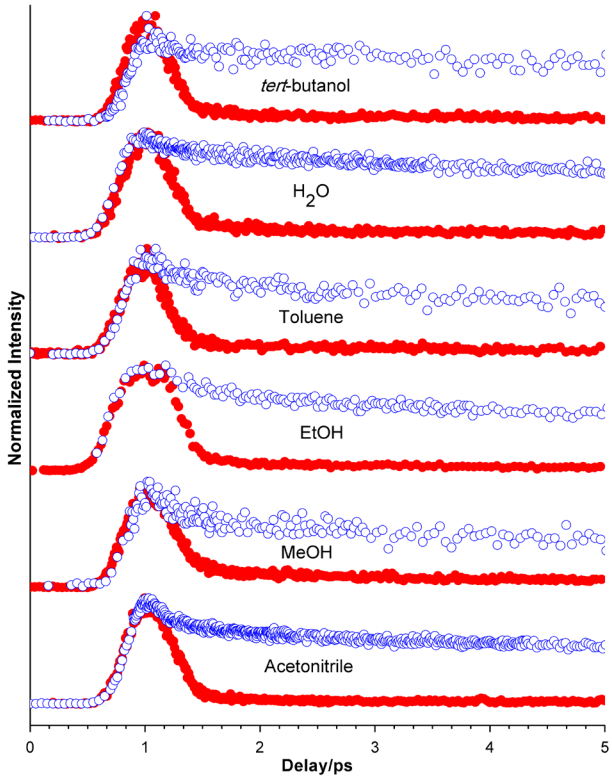

Figure 5. Femtosecond fluorescent transients of *o*-LHBPI. Excitation at 410 nm in different solvents. Red dots is emission at 475 nm and open blue circles is emission at 610 nm

The occurrence of an ESIPT is supported by the calculated PES (Fig. 6). These calculations confirm that *Z*-*o*-LHBPI (τ = 180°) is more stable than the *E*-isomer (τ = 0°). Higher level calculations in water (DFT-D3//pbe0/TZVPP-COSMO) yield an estimate of 6.4 kcal/mol for the difference in energy between the two geometric isomers and an activation barrier of 30 kcal/mol (Fig. 6A; blue). In the excited state there is a somewhat lower barrier (Fig. 6A; red) and evidence for a conical intersection with the ground state at τ ~ 90°. These data predict that the *E*-isomer of *o*-LHBPI should be non-fluorescent due to a facile return to the GS at τ = 90°, which falls back exclusively to the (emissive) *Z*-*o*-LHBPI ground state.

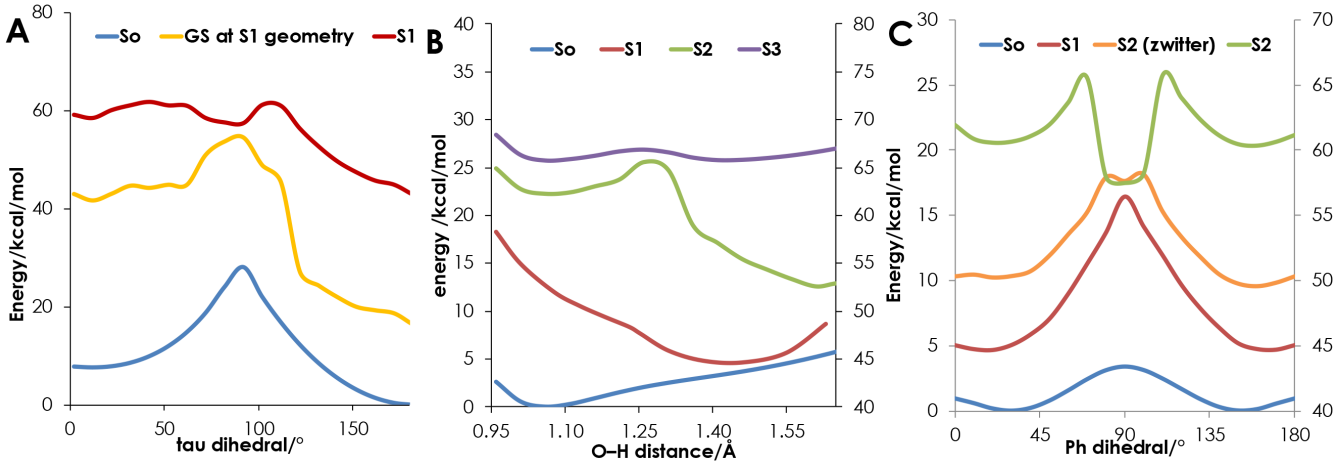

Figure 6. Potential energy surface (DFT//bp86/SV(P)) calculated for τ-bond rotation, O—H bond length and phenyl rotation in *o*-LHBPI. The ground state is in blue, the first excited state (red), second excited state (green) and third excited state in purple. The right-hand y-axis is the energy of the excited states. A) Calculated PES for *E*- (left) to *Z*- (right) isomerization at the ground (S_0) and first excited state(S_1). In gold is the PES of the ground state at the geometry of the fist excited state. B) A bond scan of the O–H bond length at the ground state (S_0) and the first three excited states (S_1-S_3). An O–H distance of 1 Å is of the neutral form and a distance of~ 1.5 Å indicates the zwitter ion (proton on nitrogen). C) Energy required for rotation of the phenyl group on its axis in the ground and first two excited states. The golden line is the PES of phenyl rotation of the zwitter ion.

In the excited state there is a much smaller barrier (~2 kcal/mol) to *E*-/*Z*-isomerism than in the ground state (*c.f.* 30 kcal/mol) and a much bigger difference between the *E*- and *Z*-isomer energies (Fig. 6A). As only the *Z*-isomer exists in solution by NMR spectroscopy (Fig. S6, Table S1), and that the *E*-isomer should be non-emissive due to the presence of a conical intersection (Fig. 6A), the dual emission must be due solely to the *Z*-isomer. This conclusion is at odds with the heterogeneity observed in the excitation spectra (Fig. 3), which suggest two species in solution.

DFT calculations show, for the global minimum (*Z*-*o*-LHBPI), that the O–H bond length is optimally 1.08 Å (Fig. 6B; blue) in the ground state. However, in the first excited state, the most stable form is with the proton on the imidazolone nitrogen, with an optimal N–H bond length of 1.07 Å (Fig. 6B, red). The steep slope and lack of any barrier in the S_1 PES (Fig. 6B) explains the lack of any rise-time seen for the 610 nm ESIPT emission (Fig. 5, Table S5). Interestingly, for the second excited state (S_2; Fig. 6B, green), the zwitter ion (proton on nitrogen) is more stable but there is a significant barrier to ESIPT of ~ 3.5 kcal/mol suggesting that S_0 – S_2 excitation does not necessarily lead to facile ESIPT.

For the red emission, a Stokes' shift of > 200 nm unambiguously assigns this emission to the ESIPT tautomer (zwitterion). The cyan emission must therefore arise from the normal FC emission (*c.f.* Fig. 4). Combining the photophysical results and DFT calculations, (Fig. 6) can explain the heterogeneity of the excitation spectra and their dependence on emission. For the global ground state (*Z*-*o*-LHBPI, τ = 180°) the exchangeable proton is on the oxygen (phenol). Upon excitation to S_1 (410 nm), there is a barrierless conversion to the N-H tautomer (imidazolium zwitter ion) that has a slow decay back to the ground state with emission at 610 nm. In contrast, excitation to the S_2 state (λ_{ex} 370 nm) there is no facile ESIPT and internal conversion back to a different region of the S_1 PES ($S_1^{\S}$) leads to FC emission (475 nm) rather than ESIPT.

According to DFT calculations, for the methyl analogue (*o*-LHBDI), the ground state and first excited states are almost planar with virtually no skeletal rearrangements required during the ESIPT (Fig. 7, Table S2). In contrast, *o*-LHBPI undergoes substantial structural rearrangement from the ground to first excited state. These include the proton moving 0.64 Å (*c.f.* 0.58 Å for *o*-LHBDI) but most notably the phenyl group must rotate over 20° (Fig. 6C) to become more planar and consequently the *N*-methyl must also rotate by 7.5° to accommodate this change. In addition, the whole π-system is now far from planar (Fig. 7), quite unlike *o*-LHBDI. This lack of planarity in *o*-LHBPI would favor a proton relay with water compared to *o*-LHBDI, explaining the large increase in quantum yield observed in water over other solvents (Table S4). This also explains the longer decay times seen for the red emission (Fig. 5, Table S5).

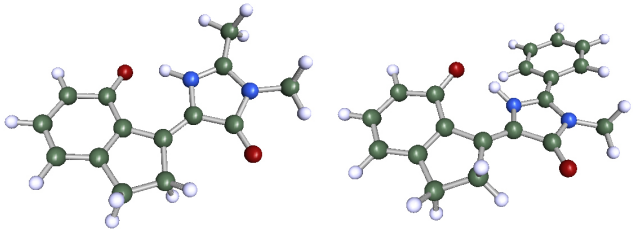

Figure 7. Global first excited state (S_1) minimum energy structures (DFT-D3//pbe0/TZVPP) for *o*-LHBDI (left) and *o*-LHBPI (right).

As has been proposed for *o*-HBDI, it is tempting to assign the ultrafast component (300 fs; Fig. 5, Table S5) found in aqueous solution of *o*-LHBPI to the vibronic relaxation of the normal form reaching thermal equilibrium.[10a] However, absence of the same component in all other solvents as well as absence of a risetime in aqueous solution does not support an ESIPT. DFT calculations (Fig. S10) show a water relayed ESPT process is possible for *o*-LHBPI. Therefore, we propose that the proton transfer process in all other solvents but water, involving an

ESIPT, is faster than the instrument's resolution (280 fs) and thus not resolved. However, water mediated ESPT process is responsible for the sub-picosecond component found in the decay trace of aqueous solution of *o*-LHBPI. Components like the 1.5 ps and 1.4 ps decays in *tert*-butanol and methanol and the 6 ps decay in water can be assigned to rotation of the phenyl group.[20] The slowest components of ~50 ps (25 ps in acetonitrile) can be assigned to the population decay time of the tautomer and is solvent dependent (Table S5).

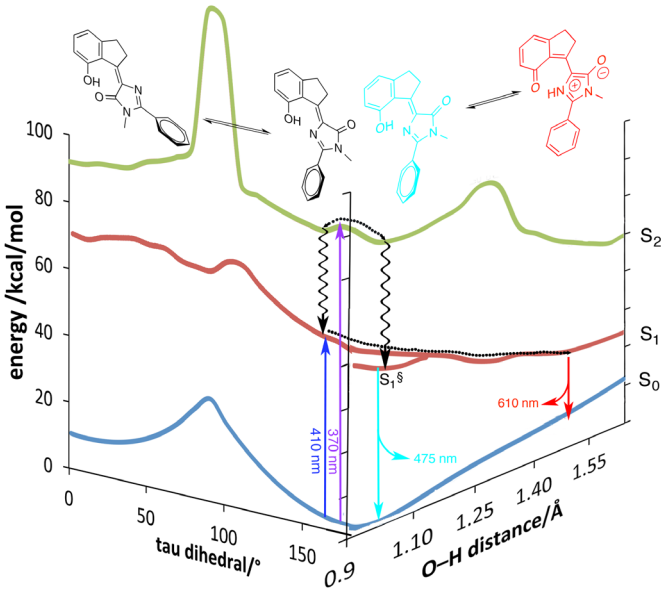

Figure 8. Schematic of excited state dynamics associated with *o*-LHBPI. Combining the observed excitation and emission profiles (Fig. 1, 3, S8-S11) with DFT calculations (Fig. 6) suggests there is a facile conversion to the zwitter ion (right) from S_1 (red line). There is a barrier to proton transfer in the S_2 state (green line) allowing it to return to S_1§, from which FC emission is possible. The two perpendicular coordinates are for τ-bond rotation and O–N proton migration. Only the (*Z*)-*o*-LHBPI is emissive and any (*E*)-*o*-LHBPI formed (left) would be efficiently converted to the *Z*-isomer in the excited state but with a 6.4 kcal/mol difference between the *E*- and *Z*-isomers no *E*-form is expected in solution.

Putting this together (Fig. 8), a plausible schematic of the excited state dynamics of *o*-LHBPI can be constructed. Upon electronic excitation of *Z*-*o*-LHBPI, to S_1 (410 nm) there is an adiabatic conversion to the zwitterionic form leading to ESIPT emission (610 nm). Conformational changes including, rotation of the phenyl group by more than 20°, shortening of the imidazolone-phenyl bond by 32 pm (hyperconjugation) as well as rotation of the *N*-methyl group by 7.5°. These make the molecule more planar and thus to facilitate ESIPT, allowing the molecule to move along the O–H–N bond coordinate. Excitation to the S_2 state (370 nm) to S_2 in contrast leads to minor structural changes and does not allow *E*-/*Z*- isomerism or ESIPT due to barriers in the S_2 PES (Figs 6, 8). The molecule spends a short time in S_2 (<280 fs; Fig. 5, Table S5) followed by an S_2 – S_1 internal conversion to S_1 or an S_1§ state, which is not on the adiabatic O–H–N PES, from which an FC emission (475 nm) can arise. From this scheme, it can also be understood why excitation with 370 nm light leads preferentially to FC emission, while excitation at 410 nm favors ESIPT. In the case of 410 nm excitation, the molecules need to undergo extensive torsional rearrangement to attain planarity, resulting in the majority of the population undergoing ESIPT. While with 370 nm excitation, the S_2 structure is very similar to the ground state, inhibiting the ESIPT and allowing the FC emission to predominate.[11d,21] For the phenyl rotation (Fig. 6C), calculation on the ground state show a 3.4 kcal/mol barrier for rotation of phenyl rotation but this climbs to 11.5 kcal/mol in the first excited state confirming hyperconjugation of the phenyl to the imidazolone in S_1. Interestingly, in the S_2 state (Fig. 6B) there is a barrier to the ESIPT. However, if the phenyl group rotates, it is possible to catalyse an ESIPT on the S_2 PES that also has a conical intersection with S_1 when the phenyl is a ~90° to the imidazolone ring (Fig. 6C). We propose that the size of the phenyl group (*c.f.* methyl) and hyperconjugation of the phenyl to the imidazolone (in S_1 but not S_0 or S_2) are responsible for the observed differences between *o*-LHBPI and *o*-LHBDI. That is, excitation from S_0 to S_2 lands on the green PES of Fig. 6C. Very minor structural changes occur before internal conversion back to S_1§ upon which 475 nm emission takes place. Any excess energy can lead to rotation of the phenyl group that at 70° facilitates an S_2 ESIPT, which has a conical intersection with S_1, landing on the S_1 PES (Fig. 6B) resulting in 610 nm emission.

To try to understand this better, fluorescence spectra were recorded at 77 K in ethanol and MeTHF. What was observed (Fig. 9) is that at 77 K the cyan emission is relatively more intense than at 298 K. The red emission is increased by ~30× blue shifted by 40 nm in aprotic solvent (Fig. S16A, C). The increase in intensity of the cyan emission at low temperature indicates that the ESIPT (or ESPT) requires some structural reorganization in the S_1 state, allowing more molecules to leak into the FC pathway. In protic solvent (Fig. S16B, D), the quantum yield is hardly increased suggesting that the major non-radiative pathway involves a H-transfer.

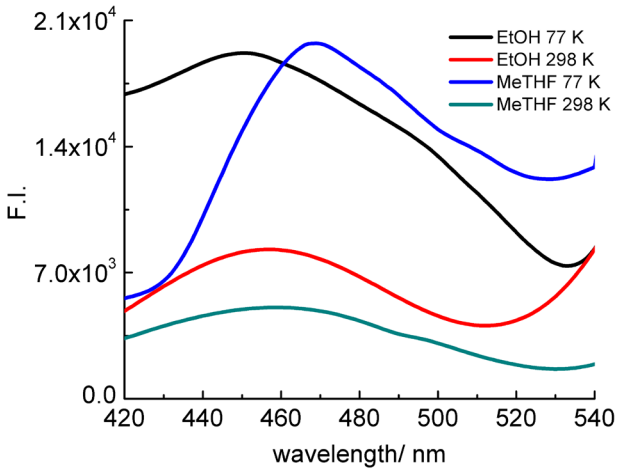

Figure 9. Emission spectra for o-LHBPI at 298 and 77 K in ethanol and MeTHF. Excitation at 370 nm showing only the cyan emission.

Ratiometric measurement of pH using *o*-LHBPI (Fig. 12) showed that the ratio between 475 nm and 615 nm fluorescence could be used to accurately measure the pH in the range 10-13. There was >10-fold difference between the respective emissions over this range. As the absorption of spectrum of *o*-LHBPI does not change with pH (except due to decomposition at very high pH; Fig. S12), we were not able to measure the pK_a using ground state spectroscopy. However, we have calculated the

pK_a* using the fluorescence emissions at 475 and 610 nm with excitation at 370 or 410 nm. In each case there is a single pK_a at ~ 9 (Fig. S15).

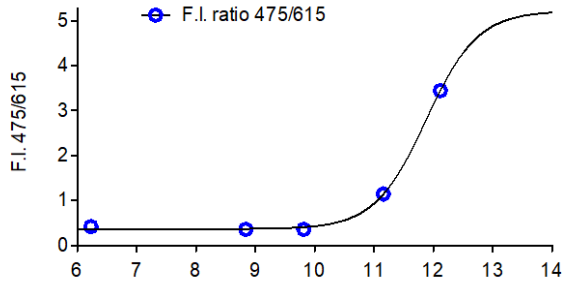

Figure 10. Ratiometric measurement of pH; plot of the ratio of F.I. (475nm/615 nm) against pH. λ_{ex} = 370 nm fitted to a standard sigmoidal dose/response curve (Hillslope = 1, r^2 = 0.9993).

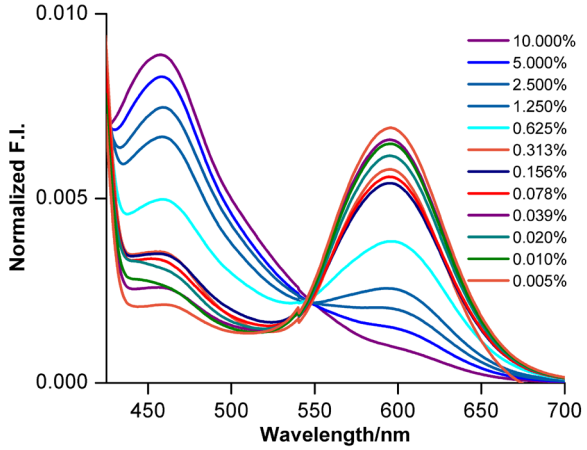

Figure 11. Area normalized emission spectra of *o*-LHBPI with increasing SDS. [SDS], 0.005 – 10 % in distilled water, pH 5.1, λ_{ex} = 365 nm.

Similarly, *o*-LHBPI gave an excellent ratiometric response to lipid concentration (Fig. 11). At low concentrations, as in water, the red emission dominates but as the SDS concentration increases, the cyan emission dominates to a point where there is virtually no red emission at 10% SDS. This is similar to the emission spectrum in acetonitrile, a solvent with detergent-like properties. These results suggested that *o*-LHBPI could be used for ratiometric measurements of biomolecules so this was investigated further.

It was also found that *o*-LHBPI could be used for sensitive ratiometric measurements of protein, lipids, polysaccharide and glycoprotein (Fig. 12) but not DNA (data not shown). To investigate the changes in fluorescence with biomolecules, 10× dilutions of protein (BSA), lipid (SDS), polysaccharide (soluble starch) and glycoprotein (fetuin) were mixed with a constant amount of *o*-LHBPI. A log-log plot then provides a measure of linearity of fluorescence response to biomolecule over a large range of concentrations. It is evident (Fig. S17, S18) that with increase in the concentration of the biomolecules, both cyan emission as well as red emission increases, irrespective of the excitation wavelength (except for SDS, where red emissions remain almost unchanged). However, an area normalized emission spectra (Figs 11, S17) reveals a pseudo-isoemissive point (except in BSA). The increase in emission intensity cannot be clearly rationalized as it may be a function of the polarity, viscosity, trapping of the molecule inside the protein etc. However, it is observed that the extent of increase is more prominent for cyan emission with respect to the red emission, irrespective of the excitation. This suggests that the S_2-S_1 internal conversion process is predominantly affected and becomes slower, leading to enhancement in the FC emission. However, the formation of zwitterion, leading to red emission, is also affected but the majority of the excited molecules undergo normal/FC emission. This can be rationalized as the higher viscosity inside a micelle or inside the glycan layer of fetuin or in hydrophobic pockets on BSA hinders phenyl ring rotation (Fig. 12) so that more of the molecules undergo S_2-S_1[§] internal conversion as opposed to phenyl rotation as ESIPT from the S_2 state.

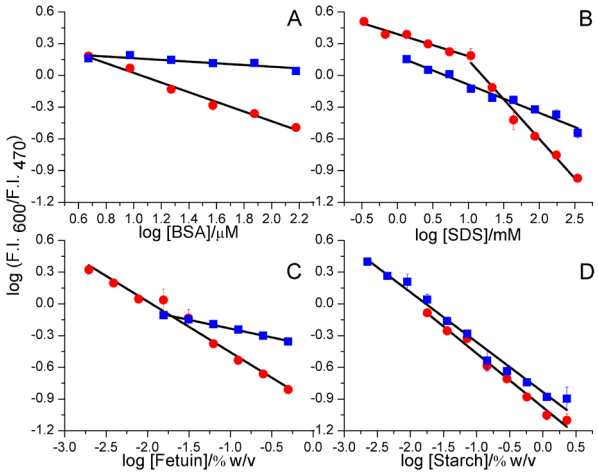

Figure 12. Ratiometric quantification of biomolecules in solution. Plots of log(600 nm:470 nm emission) against A) log([BSA]/mmol); B) log([SDS]/mmol); C) log([Fetuin]/%w/v); and log([Starch]/ %w/v). The red circles are excitation at 365 nm and the blue squares are excitation at 410 nm. The lines correspond to the best linear fitting obtained for the ratio between cyan (470 nm) and red (600 nm) emission. All solutes were dissolved in PBS, pH 7.4 except SDS, which was in water, pH 5.1.

Bovine serum albumin (BSA) was used as a model protein to determine if it was possible to measure the concentration of protein in solution ratiometrically using *o*-LHBPI. The ratio between 600 nm and 470 nm emission, with excitation at 365 nm, decreased from 2:1 to ~1:2 over the range 4-140 mM and showed a linear correlation when a log-log plot was constructed (Fig. 12A), indicating that this fluorophore can be used to accurately measure low concentration of protein in solution that is independent of many experimental variables. On the other hand, excitation at 410 nm, a similar linear correlation was found for log-log scale but the effect of change in protein concentration on the ratio of different emission intensities was not as prominent (Fig. 12A, blue squares).

As the internal hydrogen bonding in *o*-LHBPI can be affected by the availability of external hydrogen bonding sources (*e.g.* water), it was important to look at the ratio between cyan and red fluorescence in a more hydrophobic environment. From a biological perspective, lipid membranes are very hydrophobic

with ~4% water content and this can be mimicked with a detergent such as SDS, which forms micelles at 8.2 mM (CMC; Critical Micelle Concentration) in water. Membranes are also more viscous than water. Our results showed a 15-fold difference between red and cyan emission with respect to SDS concentration (Fig. 12B). This result is in line with our other observations that in non-polar solvents, the FC emission is favored over ESIPT emission, resulting in a dominant cyan emission with increasing SDS concentrations. These results, taken together suggest that this probe could be used in super resolution microscopy to measure membrane formation, fluidity and viscosity, characteristic that are difficult to measure by other means. For the 365 nm excitation, the effect of SDS concentration was distinctive, with a point of inflection at the CMC (Fig. 12B), after which the cyan emission increased rapidly by virtue of increased viscosity in the micelles. The red emission (600 nm), on the other hand did not show a sharp increase to the CMC, as a result of a more hydrophobic environment and then increased after CMC due to increase in viscosity (Fig. 12C) but not as rapidly as the cyan emission increased. This can be rationalized as destabilization of the zwitterionic form with increasing hydrophobicity and after the CMC this destabilization is increased in rate by a rapid increase in viscosity and hydrophobicity as micelles are formed.

Glycoproteins are important surface proteins on cells responsible for cell-cell recognition and integrity. The ability to specifically measure glycoproteins is an unmet need in biology. We looked at bovine fetuin, a heavily glycosylated protein, and found that an increase in fetuin concentration resulted in a linear increase in the ratio between red and cyan emissions and showed that it is possible to quantify the amount of a glycoprotein in solution (Fig. 12C). In this case too, the effect was found to be more prominent for excitation at 365 nm than 410 nm one.

The interesting results for a glycoprotein (fetuin) suggested that it might be possible to use ratiometric quantification on other types of glycans. To test this, we made a serial dilution of soluble starch. In a similar response to that observed with fetuin, a log-log plot of the concentration of starch vs. the red:cyan emission ratio revealed an extraordinary linear plot over 3 orders of magnitude (Fig. 12D). In this case there was little difference between excitation at 365 nm or 410 nm.

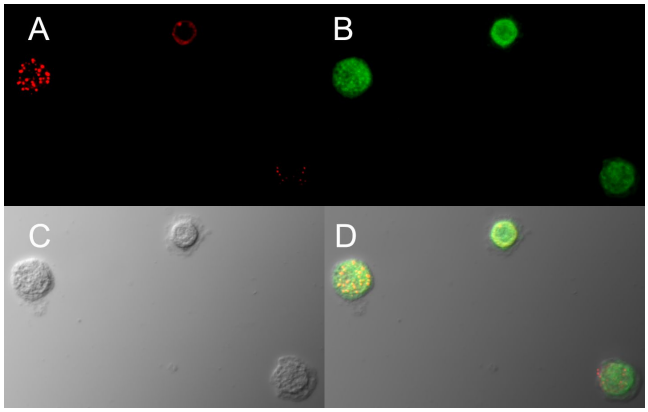

Figure 13. Confocal microscope image of SW480 cells stained with *o*-LHBPI (10 μg/mL, 30 min in PBS), washed twice with PBS and imaged on an Olympus FV1000 (λ_{ex} = 405 nm). A) λ_{em} = 580-630 nm (red) and B) λ_{em} = 440-530 nm (green) . C) Differential interference contrast (DIC) image and D) a Merge of A, B and C showing co-localization (yellow).

Finally, we looked at the ability for o-LHBPI to stain live cells. The dye was found to rapidly enter live human cells grown in culture (Fig. 13). Excitation with a 405 nm diode laser resulted to dual emission. The cyan emission (440-530 nm bandpass) false coloured green (Fig. 13B) was relatively homogeneous whereas the red emission (580-630 nm bandpass) was localized in vesicles around the perimeter of some cells (Fig. 13A). This difference can be understood in terms of Fig. 12 where the ratio of cyan to red emission can be altered in response to biomolecules. Thus o-LHBPI is picking up differences to the chemical composition of the vesicles (Fig. 13A) compared to the rest of the cell, allowing ratiometric sensing in real-time applications to be developed. The dye showed no signs of toxicity in this cell line with the concentration used (10 μg/mL). Stronger red emission was found under acidic pHs (Fig. S12) whereas lipophilic environments favored cyan emission (Fig. S17, S18). It seems reasonable to postulate that the vesicles in Fig. 13A could be lysosomes (pH 4.5-5, *c.f.* cytosol at pH 7.2). While it is beyond the scope of this paper to determine exactly what these organelles are, it is evident that dual emission from a single fluorophore is sufficiently differentiated in live cell imaging to justify further development in the area of real-time applications.

CONCLUSIONS

In summary, the effect of phenyl substitution in the *o*-locked GFP chromophore analogue, *Z*-*o*-LHBPI, was found to be non-trivial. The fluorescence quantum yield is lower than the methyl-substituted analogue because rotation of the phenyl ring provides an additional nonradiative channel of deactivation. Unlike the methyl-substituted analogue reported recently by Chou and co-workers[8a] dual emission is observed at room temperature, indicating a hindrance to the ESIPT process that leads to the formation of the red emissive phototautomer. This observation is rationalized with high level DFT calculations that indicate that, unlike *o*-LHBDI, *o*-LHBPI requires significant structural rearrangement in the excited state zwitter ion leading to a mixture of Franck-Condon normal emission and excited state proton transfer emission with an apparent Stokes' shift of >200 nm. The higher quantum yield in water indicates that H-bonding facilitates the ESIPT and this would be a useful design motif for applications in aqueous environments. As initial validation we have shown a linear correlation between biological analytes (*e.g.* protein, glycans and lipids but not DNA) and the ratio between FC and ESIPT emissions. This could be used for ratiometric quantification or in confocal/super resolution microscopy. We have shown that human cell lines can be rapidly stained with *o*-LHBPI and that there is a considerable difference between the staining pattern of the cyan and red emissions suggesting real time ratiometric observations could be useful in following developmental changes in live cells.

The results presented here open the door to using GFP chromophore analogues in biotechnological applications. For example, it can be envisaged that *o*-LHBPI analogues can be used to report on the local environment through super sensitive ratiometric comparison of the cyan and red emissions or to prepare chemically tunable optoelectronic devices.

EXPERIMENTAL

Synthesis and Characterization. Unless otherwise stated, all chemicals and reagents were received from Sigma-Aldrich (Castle Hill, Australia) and used without further purification. Dichloromethane, diethyl ether, ethanol, ethyl acetate, light petroleum, methanol, tetrahydrofuran and toluene were obtained

from ChemSupply (Australia). HPLC grade acetonitrile was obtained from BDH/Merck (Germany), and was used without further purification. Spectroscopy grade acetonitrile from Spectrochem was distilled over CaH_2 and the distillate passed through activated neutral alumina immediately prior to use. Spectroscopy grade *tert*-butanol from Spectrochem, Mumbai, India was used as received. ^{1}H NMR and ^{13}C NMR spectra were recorded in 5 mm Pyrex tubes (Wilmad, USA) on either a Bruker Avance DPX-400 400 MHz or AVII-600 600 MHz spectrometer. All spectra were obtained at 25 °C, processed using Bruker Topspin 3.2 and referenced to residual solvent ($CDCl_3$ 7.26/77.16 ppm; DMSO-d_6 2.49/39.8 ppm). Infrared spectra were taken on a Perkin Elmer paragon 1000PC FTIR spectrometer, or Nicolet iS80 FT-IR Spectrometer (Thermo Scientific, Australia). Low resolution mass spectrometry was performed by electrospray ionization (ESI) MS in positive or negative polarity mode as required on a Shimadzu LC-20A prominence system coupled to a LCMS-2010 EV mass spectrometer using LCMSsolution 3.21 software. LC-MS experiments were carried out on a Gemini C18 column (Phenomenex, Australia) 150.0 × 2.00 mm, 110Å, 3 µm. High resolution mass data were obtained from ESI in positive polarity mode on a Waters Q-TOF Ultima Tandem Quadrupole/Time-of-Flight ESI mass spectrometer, performed by the Mass Spectrometry Unit at the University of Illinois, USA. Melting point was measured using DSC 2010 differential scanning calorimeter from TA instruments. pH was measured using (ISFETCOM, model S2K712, JAPAN) pH meter. Microwave reactions were carried out using a CEM Discover system.

3-oxo-2,3-dihydro-1H-inden-4-yl acetate. 7-Hydroxy-2,3-dihydro-1*H*-inden-1-one (0.5 g, 3.37 mmol) was added to acetic anhydride (5 mL) and 2 equivalent of sodium acetate (0.55 g, 7.74 mmol). The reaction mixture was irradiated in a microwave reactor for 3 min (300 W, 140 °C). The mixture was then poured in ice/water and extracted with ethylacetate. The organic layer was washed thoroughly with water (4 × 25 mL) and concentrated *in vacuo*. Purification by flash chromatography gave the pure 7-acetoxyindanone (0.62 g, 97%), as white crystals, m.p. 76 °C [lit.[22] m.p. 75-77 °C]. ^{1}H NMR (400 MHz, $CDCl_3$) δ 7.58 (t, *J* = 7.80 Hz, 1H), 7.33 (d, *J* = 8.00 Hz, 1H), 6.97 (d, *J* = 7.70 Hz, 1H), 3.13 (t, *J* = 5.90 Hz, 2H), 2.66 (t, *J* = 5.90 Hz, 2H), 2.39 (s, 3H).

2-phenyloxazol-5(4H)-one (phenyloxazolinone). Phenyloxazolinone was synthesized by previously reported procedure.[23] Briefly, Hippuric acid (5.0 g, 27.9 mmol) and EDCI·HCl (7.0 g, 36.3 mmol) were dissolved in CH_2Cl_2 (50 mL) and stirred at room temperature for 45 min under a N_2 atmosphere. The reaction was quenched with water. The organic layer was separated, and washed twice with water and once with brine, dried over anhydrous magnesium sulfate, filtered and concentrated *in vacuo* to afford *phenyloxazolinone* as an off-white solid (4.1 g, 91%), which was used for the next reaction without further purification. ^{1}H NMR (600 MHz, $CDCl_3$) δ 7.96 (dd, J = 5.2, 3.3 Hz, 2H), 7.55 (m, 1H), 7.46 (m, 2H), 4.38 (s, 2H); ^{13}C NMR (151 MHz, $CDCl_3$) δ 176.0, 163.5, 132.9, 129.09, 128.9, 128.7, 127.9, 125.9, 77.4, 77.2, 76.9, 55.0.

(Z)-3-(5-oxo-2-phenyloxazol-4(5H)-ylidene)-2,3-dihydro-1H-inden-4-yl acetate (o-AcBPA). THF (10 mL) was chilled under N_2 to –10 °C. To it, $TiCl_4$ (0.23 mL, 2.20 mmol) in CH_2Cl_2 (0.2 mL) was added and stirred for 10 min. To the stirring solution, 3-oxo-2,3-dihydro-1*H*-inden-4-yl acetate (*7-acetoxyindanone*; 0.1 g, 0.53 mmol) was added and the mixture was stirred for 5 min, then 2-phenyloxazol-5(4H)-one (*phenyloxazolinone*, 0.13 g, 0.85 mmol) was added and stirred for a further 40 min. To the mixture, pyridine (0.17 mL, 2.20 mmol) was added dropwise. The black mixture was stirred for a further 5 hours and was monitored by TLC until the starting material had disappeared. The reaction was then quenched with saturated ammonium chloride solution (3 mL) and extracted with ethyl acetate (3 × 10 mL). The combined organic layer was washed thoroughly with water (4 × 10 mL) then brine solution (2 × 10 mL) and concentrated under vacuum. The oxazolone was purified by flash chromatography and recrystallized from methanol/water to yield a yellow solid (0.071 g, 40%), m.p. 192 °C; UV (acetonitrile) λ_{max} 365 nm (ε = 36800); IR (ATR) ν_{max} 1790, 1780, 1751, 1640 cm^{-1}; ^{1}H NMR (400 MHz, $CDCl_3$) δ 8.07 (m, 2H), 7.53 (m, 4H), 7.30 (d, *J* = 7.50 Hz, 1H), 7.06 (d, *J* = 7.87 Hz, 1H), 3.49 (t, *J* = 5.90 Hz, 2H), 3.18 (t, *J* = 5.90 Hz, 2H), 2.24 (s, 3H); ^{13}C NMR (125 MHz, $CDCl_3$) δ 169.3, 167.0, 153.6, 153.5, 148.2, 133.5, 132.8, 131.6, 129.1, 128.1, 126.2, 123.06, 122.11, 32.68, 31.43, 22.12;MS (ESI) *m/z* 334; HRMS (ESI) calcd. for $C_{20}H_{16}NO_4$ *m/z* 334.1073 [M+H$^+$], found *m/z* 334.1079.

(Z)-5-(7-hydroxy-2,3-dihydro-1H-inden-1-ylidene)-3-methyl-2-phenyl-3,5-dihydro-4H-imidazol-4-one (o-LHBPI). To the stirred solution of (*Z*)-3-(5-oxo-2-phenyloxazol-4(5*H*)-ylidene)-2,3-dihydro-1*H*-inden-4-yl acetate (*o-AcBPA*; 0.1 g, 0.3 mmol) was added a solution of sat. methylamine in water (40%; 100 µL) and K_2CO_3 (0.04 g, 0.3 mmol) and the solution refluxed for 3 h and poured onto ice (2 g). The aqueous layer was neutralized (0.1 M HCl), extracted with ethyl acetate (2 × 10 mL) and the combined ethyl acetate extracts washed with water (3 × 5 mL). The crude was purified by flash chromatography (hexane/ethyl acetate) to yield a yellow oil. The resultant oil was finally purified by HPLC (Fig. S1) using ACN/water (70:30) to obtain the final imidazolone (0.037 g, 40%) as a yellow solid, m.p. 192.5 °C; UV (acetonitrile) λ_{max} 370 nm (ε = 18600), 410 nm (ε = 21200) nm; IR (ATR) ν_{max} 1686 cm^{-1}; ^{1}H NMR (600 MHz, $CDCl_3$) δ 14.87 (s, 1H, -OH), 7.78 (d, *J* = 7.25 Hz, 1H, -CH_{ar}), 7.56 (m, 3H, -CH_{ar}), 7.35 (t, *J* = 7.73 Hz, 1H, -CH_{ar}), 6.87 (d, *J* = 7.38 Hz, 1H, -CH_{ar}), 6.80 (d, *J* = 8.20 Hz, 1H, -CH_{ar}), 3.49 (t, *J* = 5.81 Hz, 2H, -CH_2), 3.45 (s, 3H, -NCH_3), 3.18 (t, *J* = 7.73 Hz, 2H, -CH_2); ^{13}C NMR (150 MHz, $CDCl_3$) δ 167.9, 157.4, 156.9, 154.3, 153.4, 135.5, 131.6, 129.3, 128.4, 128.3, 127.5, 125.6, 116.1, 115.8, 31.3, 30.9, 29.1; MS (ESI) *m/z* 305; HRMS (ESI) calcd. for $C_{19}H_{17}N_2O_2$ *m/z* 305.1295 [M+H$^+$], found *m/z* 305.1290.

Solution Structure. The structure of *o*-LHBPI in chloroform was investigated by 2D NOESY spectroscopy in $CDCl_3$. An nOe build-up curve (Fig. S6) was constructed to determine if there was any spin diffusion with mixing times of 100-400 ms. NOESY spectra for mixing times of 100, 200 and 400 ms were acquired, cross-peaks integrated and the distances calculated (integral α $1/r^6$) for all mixing times (Table S1). The H4-H5 distance (2.50 Å based on DFT calculations) was used as a reference.

Density Functional Theory Methods. DFT calculations were carried out using Turbomole 7.1 (Cosmologic GmbH).[24] Structures were first built in MOE 2016.10 and the lowest energy conformation (LowModeMD) using the MMFF94x forcefield for energy minimization.[25] The lowest energy conformations corresponding to (*Z*)-*o*-LHBPI and (*E*)-*o*-LHBPI were used as starting structures for the DFT calculations. Structures were energy minimized (DFT//bp86/SV(P) then DFT-

D3//pbe0/TZVPP-COSMO) using ε = 80.1 and n = 1.333 to simulate water (Table S2). All ground states were confirmed by frequency analysis. TD-DFT//pbe0/TZVPP calculations were used to predict excited state conformation (Fig. 9) and calculate the theoretical UV spectra. The 5 lowest energy transitions were calculated and the rotary strengths and oscillator strengths were used to plot the theoretical UV spectrum (Table S3). Gaussian broadening with an 8 nm standard deviation and a 10 nm offset was applied to simulate experimental UV spectra (Fig. 2). A broadening of 35 nm gave a closer match to the actual UV spectrum though the oscillator strength of the 365 nm absorption is underestimated such that only one lobe of the absorption centered at 400 nm is observed. The same level of theory was used to predict the τ-rotational barrier in the ground state (Scheme S2) and the second excited state.

Bond scans (DFT//bp86/SV(P)), were used to predict the barrier to τ-bond rotation in the ground, first and second excited states (Fig. 6). Calculations were performed by incrementing the τ-angle from Z- to E- in 5° increments and optimizing the structure of the ground state or first/second excited states. Ground state energy at the first excited state geometry was performed by single point calculations (DFT//bp86/SV(P)). Similarly, an O-H bond scan was used to predict the barrier to tautomerization in the ground, first second and third excites states (Fig. 7).

Steady state absorption spectra were recorded on a JASCO V-530 double beam absorption spectrophotometer with a slit width of 1.0 nm at room temperature (Figs 1, S8, Table S4). Low μM solutions of the *o*-LHBPI in neat solvents were prepared and the absorbance (A) kept below 0.1 to prevent inner filter effects.

Steady state emission spectra were recorded on a Horiba FluoroMax-4 photon counting fluorimeter using the same solutions used for absorption measurements. with slit width of 5.0 nm for both excitation and emission monochromators. All experiments were carried out at 25 °C by using double distilled water and solvents. The emission spectra obtained were corrected for changes in absorbance using equation 1.

$$\text{F. I.}^{\text{Corrected}} = \frac{\text{F.I.}^{\text{Observed}}}{(1-10^{-\text{Absorbance}})} \quad (1)$$

The emissions of *o*-LHBPI in each solvent were fitted with two Gaussian functions using Origin 8.0 software to calculate the relative contribution of each species and their respective areas were calculated (Fig. S9, Table S4). These areas represent the contribution of each peak towards the total quantum yield of the molecule.

Quantum yields (ϕ_f) were calculated using quinine sulfate (ϕ_f = 0.546) or Lucifer yellow CH (ϕ_f = 0.21) as the references for the ~365 and ~410 nm excitations using equation 2.

$$\phi_f^{abs} = \frac{\phi_f^f}{\phi_f^s} \times \phi_s^{abs} \times \frac{n_f^2}{n_s^2} \quad (2)$$

where ϕ_f^f and ϕ_f^s are the relative quantum yields of the fluorophore and the standard, ϕ_s^{abs} is the absolute quantum yield of the standard and n corresponds to the refractive index of the solvent in which the measurements are done. Addition of individual quantum yields for cyan and red fluorescence, for each individual excitation, provided the total quantum yield for the respective excitation (Table S4). The absorbance of the solutions were kept at ~1.0 for the upconversion experiments.

Time resolved fluorescence. Femtosecond upconversion (FOG 100, CDP) experiment were carried out with 370 or 410 nm excitation using the second harmonic of a mode-locked Ti-sapphire laser (Tsunami, Spectra Physics) pumped by a 5W Millennia (Spectra Physics) laser. The fundamental beam (740/820 nm) was frequency doubled in a nonlinear crystal (1 mm BBO, θ = 25°, ϕ = 90°). The fluorescence emitted from the sample was upconverted in a nonlinear crystal (0.5 mm BBO, θ = 38°, ϕ = 90°) using the fundamental beam as a gate pulse. The upconverted light is dispersed in a monochromator and detected using photon counting electronics. A cross-correlation function obtained using the Raman scattering from ethanol displayed a full width at half-maximum (fwhm) of ~280 fs. The femtosecond fluorescence decays were fitted using a Gaussian function of the same FWHM as the excitation pulse. The fluorescence decays were recorded at the magic angle polarization (54.7°) with respect to the excitation pulse on a FOG 100 fluorescence optically gated upconversion spectrometer. The resolution was in appropriate multiples of the minimum step size of the instrument, *i.e.* 0.78 fs/step (Fig. 5). The decays were analyzed and fitted by iterative reconvolution using IgorPro software (Table S5). In theory this allows interpolation up to $1/10^{th}$ the instrumental response function.

Ratiometric fluorescence responses of *o*-LHBPI to pH [H^+], protein [BSA], lipid [SDS], carbohydrate [starch] and glycoprotein [bovine fetuin] were measured on a Jasco FP-8500 spectrofluorometer. A stock solution of probe *o*-LHBPI, (1.00 mg in 1.00 mL DMSO; 3.29 mM) was prepared and an aliquot (4 μL) was diluted to 3 mL with each test solution to give a final probe concentration of 4.39 μM in the cuvette. Absorption, excitation and emission (Fig. S12, S13, S14) spectra were recorded on the same sample. The emission spectra were normalized by the area under each emission curve (Fig. S17) in order to find the pseudo-isoemissive point.

pH 2-12 universal buffer was prepared according to Carmody.[26] Solution A (boric acid 0.2 M, citric acid 0.05 M) and solution B (trisodium phosphate, 0.1 M) were mixed in the appropriate ratios to achieve pHs of 2.5, 3.5, 4.6, 5.5, 6.2, 7.3, 8.5, 9.5, 10.6, 11.5 and 12.3. Stock solution of SDS (10% w/v in distilled water), BSA (1% in PBS; pH 7.4), starch (2.3% w/v in distilled water; pH 7.4) and fetuin (1% in PBS; pH 7.4) were used. The absorbance was measured using a Jasco V-760 spectrophotometer with auto-subtraction of background. Fluorescence spectra were acquired using a Jasco FP-8500 spectrofluorometer. Each sample was scanned for its maximum excitation wavelength (max λ_{ex}) and maximum emission wavelength (max λ_{em}), keeping slit widths at 10 nm. After background subtraction, area normalized fluorescence emission spectra were plotted for excitation at 365 and 410 nm (Fig. S17). This data was also plotted as fluorescence intensity (F.I.) against analyte concentration (Fig. S18). The fluorescence intensities in Fig. S18 were used to generate the ratiometric (log(600 nm F.I./470 nm F.I. emissions) responses of *o*-LHBPI to biomolecules (Fig. 12).

Fluorescence Microscopy. All confocal microscopy was performed using an Olympus FluoView FV 1000 IX81 Instrument. Human SW480 (ATCC CCL-228, primary adenocarcinoma of the colon) were grown using standard conditions (Leibovitz's L-15 Medium with 10% foetal bovine serum). A stock solution of *o*-LHBPI (1 mg/mL) was made up in DMSO. Cells were transferred to Eppendorf tubes, washed with PBS and resuspended in PBS containing 10 μg/mL *o*-LHBPI for 30 minutes. It was found that 10 minutes was adequate to develop

strong fluorescent signal inside the cells. The cells were then washed with PBS (2×) and loaded onto a standard microscope slide and a coverslip sealed with nail polish. Confocal images were generated using a 405 nm diode laser, 400× magnification and either a 440-530 nm (green) or 570-670 nm (red) bandpass filter (Fig. 13).

ASSOCIATED CONTENT

Supporting Information. A brief discussion of the design of HBDI analogues and mechanisms of fluorescence quenching, NMR data for all compounds, DFT results, steady state absorption and fluorescence spectra. Tables of calculated values from steady state and up conversion experiments. This material is available free of charge via the Internet at http://pubs.acs.org.

AUTHOR INFORMATION

Corresponding Author

*email: peter.karuso@mq.edu.au, tel:+612 9850 8290, fax: +612 9850 8313

Present Addresses

§ IIT (ISM) Dhanbad. Dhanbad 826004, India.

Author Contributions

The manuscript was written through contributions of all authors.

Funding Sources

This research is supported by the Australian Research Council (DP0877999) to PK. S.C. acknowledges the Australian Research Council for financial support.

ACKNOWLEDGMENT

We are indebted to Prof. A. Datta for letting us use the upconversion facility at IIT Bombay and for critically reviewing this manuscript. We would like to thank Dr Arthur Chien (Macquarie University Microscopy Facility) for confocal images, Ms Crystal Semen and Dr Matthew McKay (Australian Proteome Analysis Facility) for SW480 cells and HRMS spectra respectively.

ABBREVIATIONS

GFP, wild-type green fluorescent protein; *p*-HBDI, chromophore 4-(4-hydroxybenzylidene)-1,2-dimethyl-1*H*-imidazol-5(4*H*)-one; ESPT, excited state proton transfer; deGFP, dual emission GFP; FC, normal Frank-Condon emission; ICT, intramolecular charge transfer; TICT, intramolecular charge transfer; ESIPT, excited state intramolecular proton transfer; *o*-LHBPI, (*Z*)-5-(7-hydroxy-2,3-dihydro-1*H*-inden-1-ylidene)-3-methyl-2-phenyl-3,5-dihydro-4*H*-imidazol-4-one; STORM, stochastic optical reconstruction microscopy; DFT, density functional theory; TD-DFT, time dependent density functional theory; PES, potential energy surface; CMC, critical micelle concentration; F.I., fluorescence intensity; O.D., optical density; DIC, differential interference contrast.

REFERENCES

(1) (a) Paige, J. S.; Wu, K. Y.; Jaffrey, S. R. RNA Mimics of Green Fluorescent Protein. *Science* **2011**, *333*, 642-646. (b) Chudakov, D. M.; Matz, M. V.; Lukyanov, S.; Lukyanov, K. A. Fluorescent Proteins and Their Applications in Imaging Living Cells and Tissues. *Physiol Rev* **2010**, *90*, 1103-1163. (c) Zimmer, M. Green Fluorescent Protein (Gfp): Applications, Structure, and Related Photophysical Behavior. *Chem. Rev.* **2002**, *102*, 759-782. (d) Sullivan, K. F.; Kay, S. A. *Green Fluorescent Proteins*, 1999. (e) Tsien, R. Y. The Green Fluorescent Protein. *Annu. Rev. Biochem.* **1998**, *67*, 509-544. (f) Haseloff, J.; Siemering, K. R.; Prasher, D. C.; Hodge, S. Removal of a Cryptic Intron and Subcellular Localization of Green Fluorescent Protein Are Required to Mark Transgenic Arabidopsis Plants Brightly. *Proc. Natl. Acad. Sci. U.S.A.* **1997**, *94*, 2122-2127. (g) Chalfie, M.; Tu, Y.; Euskirchen, G.; Ward, W. W.; Prasher, D. C. Green Fluorescent Protein as a Marker for Gene Expression. *Science* **1994**, *263*, 802-805.

(2) Branchini, B. R.; Lusins, J. O.; Zimmer, M. A Molecular Mechanics and Database Analysis of the Structural Preorganization and Activation of the Chromophore-Containing Hexapeptide Fragment in Green Fluorescent Protein. *J. Biomol. Struct. Dyn.* **1997**, *14*, 441-448.

(3) (a) Fang, C.; Frontiera, R. R.; Tran, R.; Mathies, R. A. Mapping Gfp Structure Evolution During Proton Transfer with Femtosecond Raman Spectroscopy. *Nature* **2009**, *462*, 200-204. (b) Stoner-Ma, D.; Jaye, A. A.; Ronayne, K. L.; Nappa, J.; Meech, S. R.; Tonge, P. J. An Alternate Proton Acceptor for Excited State Proton Transfer in Green Fluorescent Protein: Rewiring Gfp. *J. Am. Chem. Soc.* **2008**, *130*, 1227-1235. (c) Stoner-Ma, D.; Melief, E. H.; Nappa, J.; Ronayne, K. L.; Tonge, P. J.; Meech, S. R. Proton Relay Reaction in Green Fluorescent Protein (Gfp): Polarization-Resolved Ultrafast Vibrational Spectroscopy of Isotopically Edited Gfp. *J. Phys. Chem. B* **2006**, *110*, 22009-22018.

(4) (a) Hanson, G. T.; McAnaney, T. B.; Park, E. S.; Rendell, M. E.; Yarbrough, D. K.; Chu, S.; Xi, L.; Boxer, S. G.; Montrose, M. H.; Remington, S. J. Green Fluorescent Protein Variants as Ratiometric Dual Emission Ph Sensors. 1. Structural Characterization and Preliminary Application. *Biochemistry* **2002**, *41*, 15477-15488. (b) McAnaney, T. B.; Park, E. S.; Hanson, G. T.; Remington, S. J.; Boxer, S. G. Green Fluorescent Protein Variants as Ratiometric Dual Emission Ph Sensors. 2. Excited-State Dynamics. *Biochemistry* **2002**, *41*, 15489-15494.

(5) Dempsey, G. T.; Vaughan, J. C.; Chen, K. H.; Bates, M.; Zhuang, X. Evaluation of Fluorophores for Optimal Performance in Localization-Based Super-Resolution Imaging. *Nat. Methods* **2011**, *8*, 1027-1036.

(6) (a) Sung, R.; Sung, K. Insights into the Unusual Dual Fluorescence of the Ortho-Amino Analogue of Green Fluorescent Protein Chromophore. *J. Lumin.* **2018**, *202*, 163-167. (b) Sung, R.; Sung, K. Tict Excited States of O- and P-N,N-Dimethylamino Analogues of Gfp Chromophore. *J. Phys. Org. Chem.* **2018**, *31*, e3791.

(7) (a) Kollmannsberger, M.; Rurack, K.; Resch-Genger, U.; Rettig, W.; Daub, J. Design of an Efficient Charge-Transfer Processing Molecular System Containing a Weak Electron Donor: Spectroscopic and Redox Properties and Cation-Induced Fluorescence Enhancement. *Chem. Phys. Lett.* **2000**, *329*, 363-369. (b) Nagasawa, Y.; Ando, Y.; Kataoka, D.; Matsuda, H.; Miyasaka, H.; Okada, T. Ultrafast Excited State Deactivation of Triphenylmethane Dyes. *J. Phys. Chem. A* **2002**, *106*, 2024-2035.

(8) (a) Hsu, Y.-H.; Chen, Y.-A.; Tseng, H.-W.; Zhang, Z.; Shen, J.-Y.; Chuang, W.-T.; Lin, T.-C.; Lee, C.-S.; Hung, W.-Y.; Hong, B.-C.; Liu, S.-H.; Chou, P.-T. Locked Ortho- and Para-Core Chromophores of Green Fluorescent Protein; Dramatic Emission Enhancement Via Structural Constraint. *J. Am. Chem. Soc.* **2014**, *136*, 11805-11812. (b) Tang, K.-C.; Chang, M.-J.; Lin, T.-Y.; Pan, H.-A.; Fang, T.-C.; Chen, K.-Y.; Hung, W.-Y.; Hsu, Y.-H.; Chou, P.-T. Fine Tuning the Energetics of Excited-State Intramolecular Proton Transfer (Esipt): White Light Generation in a Single Esipt System. *J. Am. Chem. Soc.* **2011**, *133*, 17738-17745.

(9) (a) Demchenko, A. P. Visualization and Sensing of Intermolecular Interactions with Two-Color Fluorescent Probes. *FEBS Lett.* **2006**, *580*, 2951-2957. (b) Demchenko, A. P.; Klymchenko, A. S.; Pivovarenko, V. G.; Ercelen, S. Ratiometric Probes: Design and Applications. *Springer Ser. Fluoresc.* **2002**, *2*, 101-110. (c) Demchenko, A. P. The Concept of Λ-Ratiometry in Fluorescence Sensing and Imaging. *J. Fluoresc.* **2010**, *20*, 1099-1128.

(10) (a) Hsieh, C. C.; Chou, P. T.; Shih, C. W.; Chuang, W. T.; Chung, M. W.; Lee, J.; Joo, T. Comprehensive Studies on an Overall Proton Transfer Cycle of the Ortho-Green Fluorescent Protein Chromophore. *J. Am. Chem. Soc.* **2011**, *133*, 2932-2943. (b) Chen, K. Y.; Cheng, Y. M.; Lai, C. H.; Hsu, C. C.; Ho, M. L.; Lee, G. H.; Chou, P. T. Ortho Green Fluorescence Protein Synthetic Chromophore; Excited-State Intramolecular Proton Transfer Via a Seven-Membered-

Ring Hydrogen-Bonding System. *J. Am. Chem. Soc.* **2007**, *129*, 4534-4535. (c) Chuang, W.-T.; Hsieh, C.-C.; Lai, C.-H.; Lai, C.-H.; Shih, C.-W.; Chen, K.-Y.; Hung, W.-Y.; Hsu, Y.-H.; Chou, P.-T. Excited-State Intramolecular Proton Transfer Molecules Bearing O-Hydroxy Analogues of Green Fluorescent Protein Chromophore. *J. Org. Chem.* **2011**, *76*, 8189-8202.

(11) (a) Chang, J.; Romei, M. G.; Boxer, S. G. Structural Evidence of Photoisomerization Pathways in Fluorescent Proteins. *J. Am. Chem. Soc.* **2019**, *141*, 15504-15508. (b) Taylor, M. A.; Zhu, L.; Rozanov, N. D.; Stout, K. T.; Chen, C.; Fang, C. Delayed Vibrational Modulation of the Solvated Gfp Chromophore into a Conical Intersection. *Phys. Chem. Chem. Phys.* **2019**, *21*, 9728-9739. (c) Conyard, J.; Heisler, I. A.; Chan, Y.; Bulman Page, P. C.; Meech, S. R.; Blancafort, L. A New Twist in the Photophysics of the Gfp Chromophore: A Volume-Conserving Molecular Torsion Couple. *Chem. Sci.* **2018**, *9*, 1803-1812. (d) Ai, Y.-J.; Liao, R.-Z.; Fang, W.-H.; Luo, Y. Theoretical Studies on the Isomerization Mechanism of the Ortho-Green Fluorescent Protein Chromophore. *Phys. Chem. Chem. Phys.* **2012**, *14*, 13409-13414. (e) Rafiq, S.; Rajbongshi, B. K.; Nair, N. N.; Sen, P.; Ramanathan, G. Excited State Relaxation Dynamics of Model Green Fluorescent Protein Chromophore Analogs: Evidence for *Cis–Trans* Isomerism. *J. Phys. Chem. A* **2011**, *115*, 13733-13742. (f) Stavrov, S. S.; Solntsev, K. M.; Tolbert, L. M.; Huppert, D. Probing the Decay Coordinate of the Green Fluorescent Protein: Arrest of Cis-Trans Isomerization by the Protein Significantly Narrows the Fluorescence Spectra. *J. Am. Chem. Soc.* **2006**, *128*, 1540-1546. (g) Gepshtein, R.; Huppert, D.; Agmon, N. Deactivation Mechanism of the Green Fluorescent Chromophore. *J. Phys. Chem. B* **2006**, *110*, 4434-4442. (h) Usman, A.; Mohammed, O. F.; Nibbering, E. T. J.; Dong, J.; Solntsev, K. M.; Tolbert, L. M. Excited-State Structure Determination of the Green Fluorescent Protein Chromophore. *J. Am. Chem. Soc.* **2005**, *127*, 11214-11215. (i) Mandal, D.; Tahara, T.; Meech, S. R. Excited-State Dynamics in the Green Fluorescent Protein Chromophore. *J. Phys. Chem. B* **2004**, *108*, 1102-1108. (j) Ishii, K.; Takeuchi, S.; Tahara, T. A 40-Fs Time-Resolved Absorption Study on Cis-Stilbene in Solution: Observation of Wavepacket Motion on the Reactive Excited State. *Chem. Phys. Lett.* **2004**, *398*, 400-406. (k) Litvinenko, K. L.; Webber, N. M.; Meech, S. R. Internal Conversion in the Chromophore of the Green Fluorescent Protein: Temperature Dependence and Isoviscosity Analysis. *J. Phys. Chem. A* **2003**, *107*, 2616-2623. (l) Mandal, D.; Tahara, T.; Webber, N. M.; Meech, S. R. Ultrafast Fluorescence of the Chromophore of the Green Fluorescent Protein in Alcohol Solutions. *Chem. Phys. Lett.* **2002**, *358*, 495-501. (m) Weber, W.; Helms, V.; McCammon, J. A.; Langhoff, P. W. Shedding Light on the Dark and Weakly Fluorescent States of Green Fluorescent Proteins. *Proc. Natl. Acad. Sci. U.S.A.* **1999**, *96*, 6177-6182. (n) Todd, D. C.; Fleming, G. R. Cis-Stilbene Isomerization: Temperature Dependence and the Role of Mechanical Friction. *J. Chem. Phys.* **1993**, *98*, 269-279. (o) Saltiel, J.; Waller, A. S.; Sears, D. F. The Temperature and Medium Dependencies of Cis-Stilbene Fluorescence. The Energetics of Twisting in the Lowest Excited Singlet State. *J. Am. Chem. Soc.* **1993**, *115*, 2453-2465.

(12) (a) Chen, C.-L.; Chen, Y.-T.; Demchenko, A. P.; Chou, P.-T. Amino Proton Donors in Excited-State Intramolecular Proton-Transfer Reactions. *Nat. Rev. Chem.* **2018**, *2*, 131-143. (b) Barthes, N. P. F.; Karpenko, I. A.; Dziuba, D.; Spadafora, M.; Auffret, J.; Demchenko, A. P.; Mely, Y.; Benhida, R.; Michel, B. Y.; Burger, A. Development of Environmentally Sensitive Fluorescent and Dual Emissive Deoxyuridine Analogues. *RSC Adv.* **2015**, *5*, 33536-33545. (c) Chatterjee, T.; Mandal, M.; Mandal, P. K. Solvent H-Bond Accepting Ability Induced Conformational Change and Its Influence Towards Fluorescence Enhancement and Dual Fluorescence of Hydroxy Meta-Gfp Chromophore Analogue. *Phys. Chem. Chem. Phys.* **2016**, *18*, 24332-24342. (d) Baranov, M. S.; Lukyanov, K. A.; Borissova, A. O.; Shamir, J.; Kosenkov, D.; Slipchenko, L. V.; Tolbert, L. M.; Yampolsky, I. V.; Solntsev, K. M. Conformationally Locked Chromophores as Models of Excited-State Proton Transfer in Fluorescent Proteins. *J. Am. Chem. Soc.* **2012**, *134*, 6025-6032. (e) Voliani, V.; Bizzarri, R.; Nifosì, R.; Abbruzzetti, S.; Grandi, E.; Viappiani, C.; Beltram, F. Cis−Trans Photoisomerization of Fluorescent-Protein Chromophores. *J. Phys. Chem. B* **2008**, *112*, 10714-10722. (f) Chatterjee, T.; Mandal, M.; Das, A.; Bhattacharyya, K.; Datta, A.; Mandal, P. K. Dual Fluorescence in Gfp Chromophore Analogues: Chemical Modulation of Charge Transfer and Proton Transfer Bands. *J. Phys. Chem. B* **2016**, *120*, 3503-3510.

(13) (a) Wu, D.; Guo, W.-W.; Liu, X.-Y.; Cui, G. Excited-State Intramolecular Proton Transfer in a Blue Fluorescence Chromophore Induces Dual Emission. *ChemPhysChem* **2016**, *17*, 2340-2347. (b) Fang, X.; Wang, Y.; Wang, D.; Zhao, G.; Zhang, W.; Ren, A.; Wang, H.; Xu, J.; Gao, B.-R.; Yang, W. Synthesized Blue Fluorescent Protein Analogue with Tunable Colors from Excited-State Intramolecular Proton Transfer through an N–H···N Hydrogen Bond. *J. Phys. Chem. Lett.* **2014**, *5*, 92-98.

(14) Sharma, V.; Lansdell, T. A.; Jin, G.; Tepe, J. J. Inhibition of Cytokine Production by Hymenialdisine Derivatives. *J. Med. Chem.* **2004**, *47*, 3700-3703.

(15) Chatterjee, S.; Karuso, P. An Efficient and Concise Method to Synthesize Locked Gfp Chromophore Analogues. *Tetrahedron Lett.* **2016**, *57*, 5197-5200.

(16) Albarran, G.; Boggess, W.; Rassolov, V.; Schuler, R. H. Absorption Spectrum, Mass Spectrometric Properties, and Electronic Structure of 1,2-Benzoquinone. *J. Phys. Chem. A* **2010**, *114*, 7470-7478.

(17) (a) Das, K.; Sarkar, N.; Majumdar, D.; Bhattacharyya, K. Excited-State Intramolecular Proton Transfer and Rotamerism of 2-(2′-Hydroxyphenyl) Benzimidazole. *Chem. Phys. Lett.* **1992**, *198*, 443-448. (b) Dzugan, T. P.; Schmidt, J.; Aartsma, T. J. On the Ground-State Tautomerization of 3-Hydroxyflavone. *Chem. Phys. Lett.* **1986**, *127*, 336-342.

(18) (a) Abou-Zied, O. K. Steady-State and Time-Resolved Spectroscopy of 2,2'-Bipyridine-3,3'-Diol in Solvents and Cyclodextrins: Polarity and Nanoconfinement Effects on Tautomerization. *J. Phys. Chem. B* **2010**, *114*, 1069-1076. (b) Abou-Zied, O. K. Investigating 2,2'-Bipyridine-3,3'-Diol as a Microenvironment-Sensitive Probe: Its Binding to Cyclodextrins and Human Serum Albumin. *J. Phys. Chem. B* **2007**, *111*, 9879-9885. (c) Abou-Zied, O. K.; Al-Hinai, A. T. Caging Effects on the Ground and Excited States of 2,2'-Bipyridine-3,3'-Diol Embedded in Cyclodextrins. *J. Phys. Chem. A* **2006**, *110*, 7835-7840. (d) Chou, P.-T.; Yu, W.-S.; Wei, C.-Y.; Cheng, Y.-M.; Yang, C.-Y. Water-Catalyzed Excited-State Double Proton Transfer in 3-Cyano-7-Azaindole: The Resolution of the Proton-Transfer Mechanism for 7-Azaindoles in Pure Water. *J. Am. Chem. Soc.* **2001**, *123*, 3599-3600. (e) Wu, Y.-S.; Huang, H.-C.; Shen, J.-Y.; Tseng, H.-W.; Ho, J.-W.; Chen, Y.-H.; Chou, P.-T. Water-Catalyzed Excited-State Proton-Transfer Reactions in 7-Azaindole and Its Analogues. *J. Phys. Chem. B* **2015**, *119*, 2302-2309. (f) Tu, T.-H.; Chen, Y.-T.; Shen, J.-Y.; Lin, T.-C.; Chou, P.-T. Excited-State Proton Transfer in 3-Cyano-7-Azaindole: From Aqueous Solution to Ice. *J. Phys. Chem. A* **2018**, *122*, 2479-2484.

(19) (a) Raju, B. B.; Varadarajan, T. S. Spectroscopic Studies of 7-Diethylamino-3-Styryl Coumarins. *J. Photochem. Photobiol. A: Chem.* **1995**, *85*, 263-267. (b) Wee, K.-R.; Ahn, H.-C.; Son, H.-J.; Han, W.-S.; Kim, J.-E.; Cho, D. W.; Kang, S. O. Emission Color Tuning and Deep Blue Dopant Materials Based on 1,6-Bis(N-Phenyl-P-(R)-Phenylamino)Pyrene. *J. Org. Chem.* **2009**, *74*, 8472-8475. (c) Deng, H.; Yu, C.; Gong, L.; Zhu, X. Self-Restricted Green Fluorescent Protein Chromophore Analogues: Dramatic Emission Enhancement and Remarkable Solvatofluorochromism. *J. Phys. Chem. Lett.* **2016**, *7*, 2935-2944.

(20) (a) Zhao, G.-J.; Han, K.-L.; Lei, Y.-B.; Dou, Y.-S. Ultrafast Excited-State Dynamics of Tetraphenylethylene Studied by Semiclassical Simulation. *J. Chem. Phys.* **2007**, *127*, 094307. (b) Li, G.; Magana, D.; Dyer, R. B. Direct Observation and Control of Ultrafast Photoinduced Twisted Intramolecular Charge Transfer (Tict) in Triphenyl-Methane Dyes. *J. Phys. Chem. B* **2012**, *116*, 12590-12596.

(21) Liu, X.-Y.; Chang, X.-P.; Xia, S.-H.; Cui, G.; Thiel, W. Excited-State Proton-Transfer-Induced Trapping Enhances the Fluorescence Emission of a Locked Gfp Chromophore. *J. Chem. Theory Comput.* **2016**, *12*, 753-764.

(22) Narine, A. A.; Wilson, P. D. Synthesis and Evaluation of 7-Hydroxyindan-1-One-Derived Chiral Auxiliaries. *Can. J. Chem.* **2005**, *83*, 413-419.

(23) Izumi, S.; Kobayashi, Y.; Takemoto, Y. Catalytic Asymmetric Synthesis of Anti-A,B-Diamino Acid Derivatives. *Org. Lett.* **2016**, *18*, 696-699.

(24) Turbomole V7.1.1 2016, a Development of University of Karlsruhe and Forschungszentrum Karlsruhe Gmbh, 1989-2007; Turbomole Gmbh, since 2007. available from http://www.turbomole.com.

(25) Molecular Operating Environment (Moe 2018.10), Chemical Com-Puting Group Inc.: 1010 Sherbooke St. West, Suite #910, Montreal, Qc, Canada, H3a 2r7, 2016. available from https://www.chemcomp.com.

(26) Carmody, W. R. An Easily Prepared Wide Range Buffer Series. *J. Chem. Ed.* **1963**, *40*, A386.

SYNOPSIS TOC